Scale-up and electrochemical validation of Fe-modified Mn–Cu spinel coatings deposited by electrophoretic deposition for solid oxide cell interconnect applications

Journal of Materials Chemistry A

ROYAL SOCIETY OF CHEMISTRY

PAPER

Published on 07 August 2026

Cite this: DOI: 10.1039/d6ta04364j

Scale-up and electrochemical validation of Fe-modified Mn–Cu spinel coatings deposited by electrophoretic deposition for solid oxide cell interconnect applications

Francesco Gallo, *[a] Simone Anelli,[a] Fabiana D'Isanto,[a] Xiufu Sun,[b] Marco Castelli,[b] Antonio Gianfranco Sabato,[c] Albert Tarancón [cd] and Federico Smeacetto[a]

Received 22nd May 2026
Accepted 3rd August 2026

DOI: 10.1039/d6ta04364j

rsc.li/materials-a

Cobalt-free Mn–Cu spinel coatings, with and without Fe modification, were deposited by electrophoretic deposition (EPD) and comparatively evaluated as protective layers for solid oxide cell (SOC) interconnects. The addition of Fe_2O_3 led to a finer and more uniform microstructure, while XRD and EDS results were consistent with Fe incorporation into the Mn–Cu spinel-based phase after thermal treatment. Electrochemical testing was performed on large-area interconnects under dual-atmosphere operation (850 °C, 10% H_2 + 90% H_2O/air) for over 1300 h. The MnCuFe-coated Crofer 22 APU exhibited initial area-specific resistance (ASR) values in the range of 10–20 mΩ cm^2, followed by a moderate increase during the first few hundred hours and progressive stabilization beyond 1000 h. Post-mortem analyses revealed controlled chromia growth and preserved coating integrity. These results demonstrate the feasibility of scaling up EPD-processed Mn–Cu-based coatings and validate their performance under industrially relevant conditions, positioning them as viable cobalt-free alternatives for SOC interconnect protection.

1. Introduction

The global transition to renewable energy is accelerating, driven by the urgent need to achieve carbon neutrality and limit climate change. However, the inherent intermittency of sources such as solar and wind presents significant challenges for grid stability and the effective storage of excess energy.[1–4] Among the emerging solutions, hydrogen is increasingly recognized as a versatile energy carrier, capable of storing and transporting energy derived from renewable sources.[5]

Solid oxide cells (SOCs) have attracted considerable attention as one of the most efficient and flexible technologies for both high-temperature electricity generation (solid oxide fuel cells, SOFCs) and hydrogen production (solid oxide electrolysis cells, SOECs).[6] SOC devices combine high efficiency with fuel flexibility; however, their commercialization is hindered by durability issues arising from operation at elevated temperatures (typically 600–850 °C) under oxidizing and reducing atmospheres, often combined with high steam content and thermal or redox cycling. In particular, long-term operation is compromised by degradation phenomena affecting the metallic interconnects, primarily manufactured from ferritic stainless steel.[7–9] Chromium volatilization and the formation of electrically insulating oxide scales on metallic interconnects increase the area specific resistance (ASR) and promote chromium poisoning of the oxygen electrode, ultimately leading to progressive performance degradation.[10,11] This issue is particularly critical considering the state-of-the-art SOC configuration, which typically employs Ni-YSZ or Ni-GDC cermets as fuel electrodes, dense YSZ or GDC-based electrolytes, and perovskite-based oxygen electrodes, including LSM (mainly electronic conductor) and mixed ionic–electronic conductors such as LSCF.[12,13] While these materials ensure high electrochemical activity at intermediate-to-high temperatures, the oxygen electrode is especially susceptible to chromium deposition, which blocks active sites and accelerates performance decay.[14–17] To address these issues, protective coatings based on reactive-element oxides, rare-earth perovskites, and spinel-type oxides have been extensively investigated. These materials are applied as functional ceramic layers on metallic interconnects, where they act as chemical and physical barriers against oxidation and chromium volatilization while maintaining adequate electrical conductivity.[7,15,18–21]

The interconnect component plays a crucial role within the SOC stack, connecting electrically adjacent cells and physically

[a]Department of Applied Science and Technology, Politecnico di Torino, Corso Duca degli Abruzzi 24, 10129 Torino, Italy. E-mail: francesco.gallo@polito.it

[b]Department of Energy Conversion and Storage, Technical University of Denmark, 2800 Kgs. Lyngby, Denmark

[c]Nanoionics and Fuel Cells, Catalonia Institute for Energy Research (IREC), Sant Adrià de Besòs, 08930 Barcelona, Spain

[d]ICREA, Passeig Lluís Companys 23, 08010 Barcelona, Spain

separating the fuel and oxidant compartments. For practical designs, interconnects are often fabricated with a channelled geometry, which enhances mechanical stability, promotes homogenised gas distribution, and enables compact stacking. However, this introduces geometric complexity that poses substantial challenges for achieving uniform, conformal coatings with conventional deposition techniques.[22–26]

Electrophoretic deposition (EPD) has emerged as a promising, cost-effective, and scalable method for applying dense and compact ceramic layers to substrates with complex shapes.[15,27,28] The effectiveness of EPD coatings strongly depends on multiple factors, including suspension formulation, deposition parameters, and post-deposition heat treatments. Its versatility allows the deposition of a wide range of materials. Cobalt-based spinels currently represent the state of the art for protective coatings in SOC applications due to their electrical conductivity, high stability, and compatibility with the other materials in typical SOC operating conditions.[26,29–33] Achieving dense, adherent protective coatings based on these materials remains a critical challenge.[34,35] In addition, the effect of dopants on the sintering behaviour, electrical conductivity, and chromium-blocking properties of spinel coatings is an active research topic.[36–39]

Despite these advantages, the presence of cobalt poses environmental, health, and ethical concerns.[40] In this context, Mn–Cu-based spinels have emerged as promising materials due to their non-critical composition, lower environmental impact, and excellent chemical and thermal compatibility with SOC components.[18,19,41–44] However, Mn–Cu coatings still face critical challenges, including limited long-term corrosion data, Cu surface segregation, and a marked tendency to develop CuO-rich surface layers, secondary phases, and porous microstructures during sintering and redox treatments, if not carefully controlled, all of which can compromise phase stability and long-term protective behaviour.[41] Fe incorporation in Mn–Cu spinels has been widely investigated and reported to enhance sintering behaviour, promote densification, and stabilize the spinel structure.[43,45] However, its performance under realistic dual-atmosphere conditions and at large interconnect scale remains largely unexplored. In addition, Mazur *et al.* demonstrated that the Fe content in Cu–Mn spinels must be carefully balanced. Excessive Fe incorporation promotes the formation of secondary bixbyite or tetragonal spinel phases, increases local structural disorder and Mn^{2+}/Mn^{3+} fractions at the expense of Mn^{4+}, and leads to regions enriched in poorly conducting $Mn_2O_3^-$ and Cr-rich spinels. This ultimately lowers electrical conductivity, thickens the Cr-containing reaction layer, and increases ASR after long-term oxidation.[46] While these effects are well documented at the material level, the behaviour of Fe-modified Mn–Cu coatings under realistic SOC operating conditions, particularly under dual-atmosphere exposure and at large interconnect scale, remains largely unexplored. Furthermore, most studies reported in the literature are limited to small-scale samples and controlled laboratory conditions, and do not address the challenges associated with scaling up the deposition process to practical interconnect dimensions.

In this work, Mn–Cu spinel coatings, with and without Fe addition, are developed *via* electrophoretic deposition and comparatively evaluated. Fe addition was achieved through electrophoretic co-deposition of $Cu_{1.3}Mn_{1.7}O_4$ and Fe_2O_3, enabling control of the final composition without additional powder synthesis steps. This approach provides a scalable route for coating large-area interconnects with uniform thickness and good adhesion.[30,39] Two sintering strategies were investigated: conventional single-step oxidation and reduction–reoxidation treatment. The optimized reduction–reoxidation route (900 °C in Ar/H_2 followed by reoxidation at 900 °C) produces dense coatings (10–15 μm) with improved microstructural homogeneity.

To validate coating performance under realistic operating conditions, electrochemical testing was performed on large-area (5.3 × 5.3 cm) flat Crofer 22 APU interconnects. Area-specific resistance measurements were carried out for more than 1300 h at 850 °C under dual-atmosphere conditions. This study therefore focuses not only on material optimisation, but also on the validation of coating performance under industrially relevant conditions, including large-area components and realistic operating environments. Therefore, the novelty of this work lies not in Fe modification alone, but in the integration of Fe-modified Mn–Cu spinel chemistry with scalable EPD processing, large-area interconnect coating, long-term dual-atmosphere electrochemical validation, and post-mortem degradation analysis under SOC-relevant conditions. The results are compared with those of state-of-the-art Mn–Co-coated and uncoated substrates reported in the literature.

2. Materials and methods

2.1. Stainless steel substrates

Crofer 22 APU ferritic stainless steel was selected as the substrate material. According to supplier datasheets, its chemical composition (wt%) is approximately: Cr 20–24, Mn 0.3–0.8, Si < 0.5, Cu < 0.5, Al < 0.5, Ti 0.03–0.2, La 0.04–0.2, C < 0.03, P < 0.05, S < 0.02, Fe balance.[47] Small coupons (10 mm × 10 mm × 0.2 mm) were used for process optimization, while larger-area flat samples (5.3 cm × 5.3 cm × 0.81 mm) were prepared for long-term stability and electrochemical testing. Before deposition, substrates were degreased in acetone and ethanol (Merck KGaA) using an ultrasonic bath for 10 min.

2.2. Powders and suspension preparation

A commercial spinel powder with nominal composition $Cu_{1.3}Mn_{1.7}O_4$ (Nexceris; $d_{50} = 0.0625$ μm) was used as the base material. Fe_2O_3 powder (Fluka; $d_{50} = 0.075$ μm) was used as an iron oxide precursor and co-deposited with the Mn–Cu spinel powder by electrophoretic deposition. Both powders were used in their as-received condition, without high-energy ball milling or additional particle-size refinement. Further milling of already nanometric/submicrometric powders is challenging and may lead to uncontrolled agglomeration or modification of the particle size distribution. The presence of soft agglomerates was not considered detrimental for EPD, as the suspensions

were ultrasonicated before deposition to promote dispersion and break up weak agglomerates. Two suspensions with a solid loading of 10 g L^{-1} were prepared in a 50 : 50 vol% ethanol/acetone mixture. Iodine (1 g L^{-1}) was added as charging agent to enhance particle mobility and deposition uniformity.[48] Before deposition, the suspensions were ultrasonicated for 10 min and magnetically stirred for 10 min to promote particle dispersion.

- MnCu suspension: $Cu_{1.3}Mn_{1.7}O_4$ only.
- MnCuFe suspension: 90 wt% $Cu_{1.3}Mn_{1.7}O_4$ + 10 wt% Fe_2O_3.

The Fe_2O_3 content was selected based on literature reports indicating that moderate Fe incorporation promotes spinel stabilization and improves sintering behaviour, while avoiding the formation of secondary phases and the deterioration of electrical conductivity associated with higher Fe contents.[45,49]

2.3. Electrophoretic deposition

EPD was performed in a two-electrode configuration using Crofer 22 APU plates of identical dimensions as electrodes. The substrate to be coated was connected to the negative terminal and the counter electrode to the positive terminal. The electrodes were positioned parallel to each other at an inter-electrode distance of 10 mm.

Depositions were carried out under DC constant-voltage conditions at 30, 45, and 60 V for 60 s. After deposition, samples were dried at room temperature until complete solvent evaporation.

2.4. Sintering treatments

Two thermal treatment routes were applied to sinter Mn–Cu-based spinel coatings:

- Single-step oxidation: 900 °C for 2 h in static air, heating/cooling rate: 3 °C min^{-1}.
- Two-step process: reduction in Ar/H_2 (5 vol% H_2) at 900 °C for 2 h (5 °C min^{-1}), followed by reoxidation at 900 °C for 2 h (3 °C min^{-1}).

After the reduction step, selected samples were characterized to assess possible phase decomposition and substrate degradation. Table 1 reports the labels of the different samples.

2.5. Powder and coating characterization

Powder morphology and microstructure were analysed by field-emission scanning electron microscopy (FE-SEM, MIRA3, TESCAN) equipped with energy-dispersive X-ray spectroscopy (EDS, FESEM-EDS SUPRATM 40, Zeiss and Merlin Gemini Zeiss and MIRA3 XMH, TESCAN) for elemental analysis and mapping.

Phase composition was determined by X-ray diffraction (XRD) using a PANalytical Empyrean diffractometer with Cu Kα radiation in the 2θ range of 20–70°, with a step size of 0.013° and a counting time of 100 s per step. Phase identification was performed using HighScore software and the ICDD (International Centre for Diffraction Data, Newton Square, Pennsylvania, USA) database.

Particle size distribution was measured by laser diffraction using a Mastersizer 3000 equipped with a Hydro EV wet dispersion unit (Malvern Panalytical). Measurements were performed in water on the as-received powders. Prior to analysis, the powder suspensions were ultrasonicated for 10 min, and sonication was also applied during the measurement to minimize agglomeration.

In situ high-temperature X-ray diffraction (HSXRD) was carried out using the same diffractometer equipped with a high-temperature chamber (Anton Paar HTK1200N) to investigate the phase evolution of MnCu and MnCuFe systems during thermal treatment in air. The samples were heated from room temperature up to 950 °C at a rate of 3 °C min^{-1}. Diffraction patterns were collected at selected temperatures between 600 °C and 950 °C in 50 °C increments. A 10 min dwell time was applied at each temperature prior to data acquisition to ensure thermal stabilization. Additional measurements were performed during cooling to evaluate the reversibility of phase transformations. This analysis was used to identify phase stability limits, detect spinel decomposition, and assess whether the phase evolution was consistent with Fe incorporation into the spinel-based structure as a function of temperature.

Coating morphology and cross-sections were examined by FE-SEM/EDX. Samples were embedded in epoxy (Struers, Denmark), ground using SiC papers up to 4000 grits, polished with diamond suspensions, and sputter-coated with Pt.

2.6. Electrochemical testing

Electrochemical characterization was performed on large-area (5.3 cm × 5.3 cm) flat Crofer 22 APU interconnects under stack-relevant conditions at 850 °C. For testing, an alumina solid oxide cell test house was used; the coated plate was sandwiched between Ni and Au meshes, which served as gas distribution and electrical contact components in the fuel gas compartment and air compartment, respectively.[50] The effective contact area during measurements was 40 mm × 40 mm.

Table 1 Samples overview

Sample label	Spinel precursors	Reduction treatment	Oxidation treatment
MnCu_1S	100 wt% $Cu_{1.3}Mn_{1.7}O_4$	—	900 °C, 2 h, static air
MnCu_Red	100 wt% $Cu_{1.3}Mn_{1.7}O_4$	900 °C, 2 h, Ar/H_2, (5 vol% H_2)	—
MnCu_2S	100 wt% $Cu_{1.3}Mn_{1.7}O_4$	900 °C, 2 h, Ar/H_2, (5 vol% H_2)	900 °C, 2 h, static air
MnCuFe_1S	90 wt% $Cu_{1.3}Mn_{1.7}O_4$; 10 wt% Fe_2O_3	—	900 °C, 2 h, static air
MnCuFe_Red	90 wt% $Cu_{1.3}Mn_{1.7}O_4$; 10 wt% Fe_2O_3	900 °C, 2 h, Ar/H_2, (5 vol% H_2)	—
MnCuFe_2S	90 wt% $Cu_{1.3}Mn_{1.7}O_4$; 10 wt% Fe_2O_3	900 °C, 2 h, Ar/H_2, (5 vol% H_2)	900 °C, 2 h, static air

Durability tests were conducted under dual-atmosphere conditions, supplying 10% H_2 + 90% H_2O to the fuel side and air to the oxygen side. DC current of 2 A (0.125 A cm^{-2}) was applied, and voltages were measured in every 2 minutes for over 1300 h. ASR was calculated from the measured voltage and applied current and normalized to the effective contact area.

3. Results and discussion

3.1. Powder characterization

The commercial $Cu_{1.3}Mn_{1.7}O_4$ spinel powder, used in its as-received condition, was characterized prior to deposition. The morphology, crystalline structure, and particle size distribution are shown in Fig. 1a–c. FE-SEM observations reveal irregularly shaped particles (Fig. 1a), while XRD analysis (Fig. 1b) confirms the presence of a single-phase cubic spinel structure, with no detectable secondary phases. The particle size distribution (Fig. 1c) exhibits a bimodal behaviour, with $d_{50} = 0.0625$ μm and $d_{90} = 0.204$ μm. The nanometric particle size contributes to suspension stability, promoting homogeneous dispersion and limiting sedimentation during EPD. Moreover, the observed bimodal distribution may be beneficial for EPD coating formation rather than detrimental. Previous studies on EPD-processed spinel protective coatings have shown that properly balanced multimodal particle size distributions can improve particle packing, as finer particles may fill the interstitial spaces between coarser particles, leading to denser coatings and improved functional properties.[51,52] For this reason, the as-received powder was considered suitable for deposition.[53,54]

The same set of characterization techniques was applied to the iron oxide powder to evaluate its compatibility and possible reactivity with the spinel phase during the subsequent processing steps. Results are shown in Fig. 1d–f. The same characterization was performed on the Fe_2O_3 powder (Fig. 1d and f). The particles exhibit a nearly spherical morphology (Fig. 1d), and XRD confirms the presence of a single iron oxide phase (Fig. 1e). The particle size distribution (Fig. 1f) indicates the presence of soft agglomerates, which may influence suspension stability and particle packing during deposition.

The powders were first investigated separately in suspension to determine their electrophoretic behaviour and the sign of their surface charge under the selected solvent system. Both MnCu and Fe_2O_3 particles exhibited a positive surface charge, leading to preferential deposition on the negatively biased electrode, in agreement with the literature.[19]

To investigate the thermal behaviour of the $Cu_{1.3}Mn_{1.7}O_4$ spinel powder, HSXRD analyses were carried out, as shown in Fig. 2a and b. This analysis aimed to identify any phase transitions or structural changes in the spinel powder across the investigated temperature range under conditions relevant to the subsequent thermal treatment. As expected, the increasing temperature shifted the XRD peaks toward lower diffraction angles, consistent with lattice expansion according to Bragg's law. Under the temperature resolution of the HSXRD experiment, CuO-related reflections were first clearly detected at 800 °C, indicating that detectable CuO formation occurs between 750 and 800 °C. Since CuO is not present in the initial powder, its formation suggests partial decomposition or cation redistribution within the Cu–Mn–O system. This behaviour is consistent

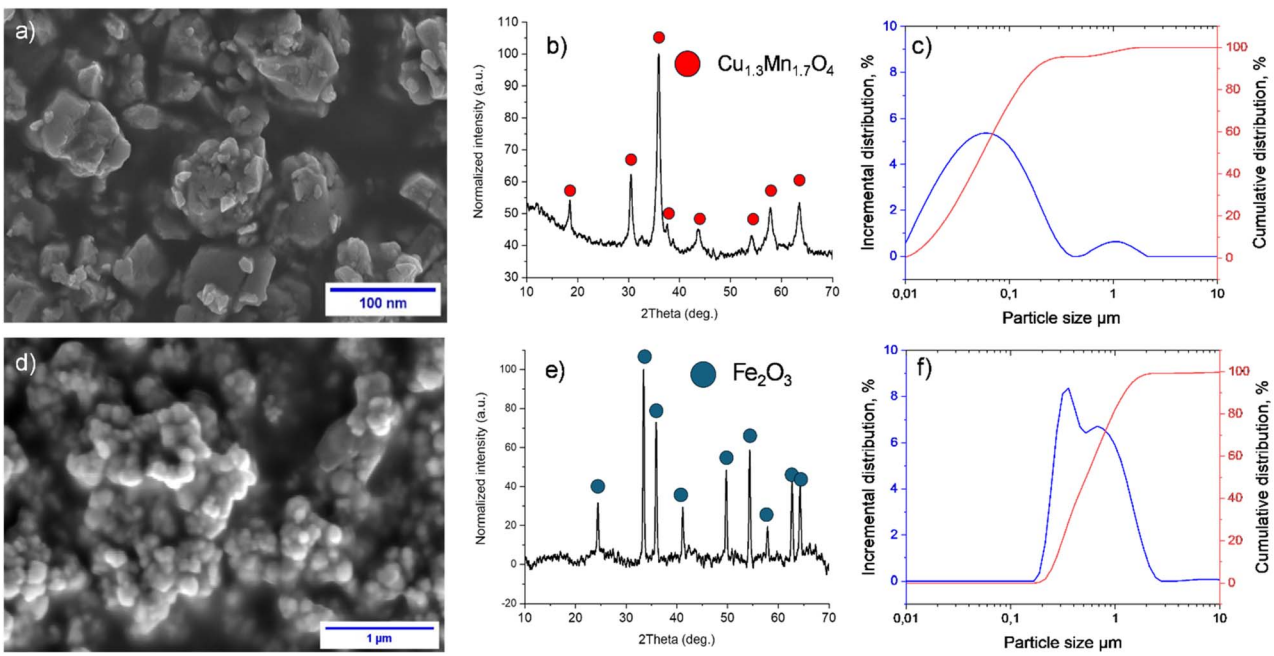

Fig. 1 Analysis of MnCu-based spinel powder and Fe_2O_3 powder: (a) FE-SEM micrograph showing particle morphology MnCu; (b) X-ray diffraction pattern with phase identification MnCu; (c) particle size distribution determined by laser scattering MnCu (d) FE-SEM micrograph showing particle morphology Fe_2O_3; (e) X-ray diffraction pattern with phase identification Fe_2O_3; (f) particle size distribution determined by laser scattering Fe_2O_3.

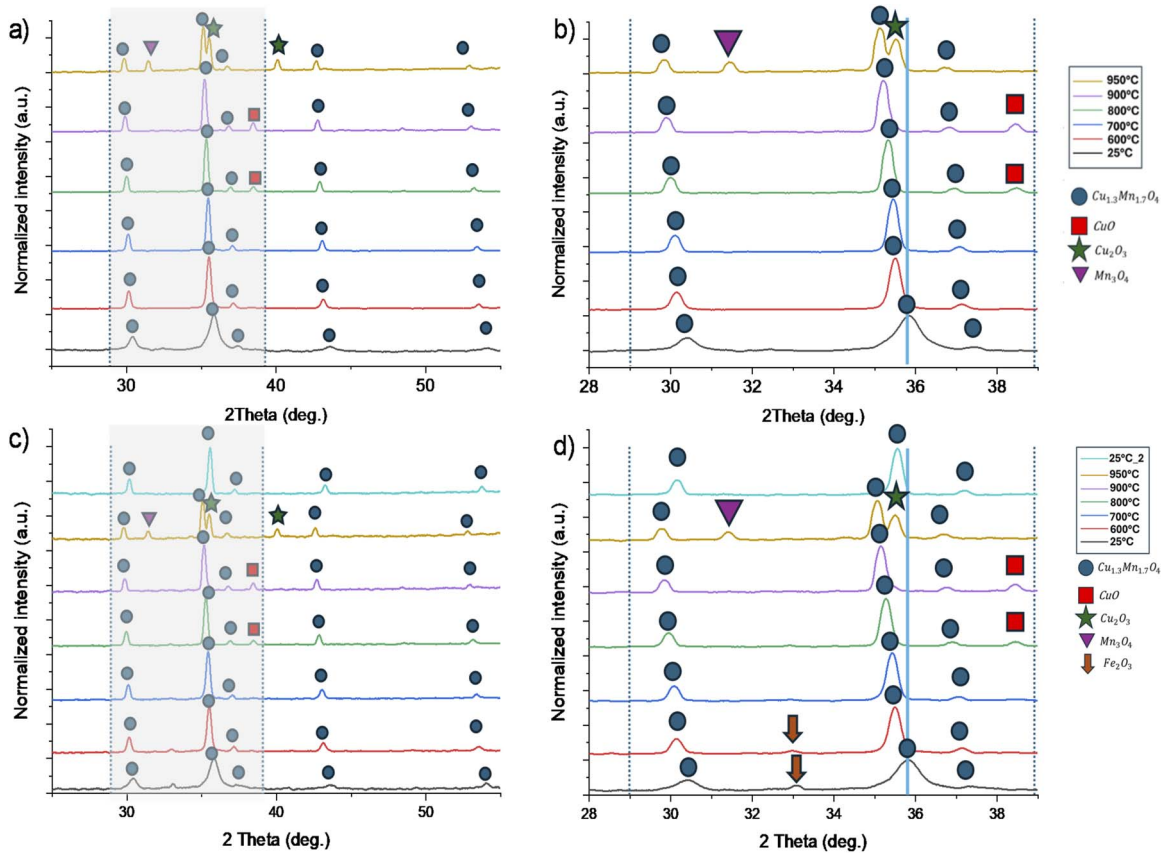

Fig. 2 X-ray diffraction patterns of MnCu-based spinel powder and MnCuFe powder with phase identification at different temperatures (a) MnCu, $2\theta = 25–55°$ (b) MnCu, $2\theta = 28–39°$ (c) MnCuFe, $2\theta = 25–55°$ (d) MnCuFe, $2\theta = 28–39°$.

with the Cu–Mn–O phase diagram, which predicts destabilization of the spinel phase and the formation of CuO-containing assemblages at elevated temperatures.

Complementary TGA-DSC analysis performed on the MnCuFe powder mixture showed a slight change in the slope of the TGA curve at approximately 750 °C, supporting the onset of thermal evolution in the same temperature range where CuO-related reflections were detected by HSXRD. Since no sharp DSC peak was observed, the transformation is interpreted as gradual, and the HSXRD results remain the primary evidence for CuO formation.

At 950 °C, a more pronounced modification of the diffraction profile is observed, further supporting the progression of this transformation.[55] To evaluate the interaction between the spinel matrix and the iron oxide dopant HSXRD was performed on a powder mixture containing 90 wt% spinel and 10 wt% iron oxide simulating the intended doped coating configuration. In the Fe-containing sample, labelled MnCuFe, shown in Fig. 2c and d, the room-temperature XRD pattern reveals distinct Mn–Cu spinel and Fe_2O_3 phases. In particular, the presence of the characteristic Fe_2O_3 peak at 33.47° confirms that the iron oxide originates from the added precursor and is effectively present in the starting mixture. Upon heating to 600 °C, the gradual disappearance of Fe_2O_3 peaks indicates progressive reaction of the iron oxide precursor with the Mn–Cu spinel phase. This is further supported by a systematic shift of the main spinel peaks toward lower angles, consistent with lattice-parameter modification associated with Fe incorporation into the spinel-based structure. Importantly, the XRD pattern collected after cooling back to 25 °C shows no reappearance of Fe_2O_3 peaks, indicating that no phase re-separation occurs upon cooling. These results support the stable incorporation of iron into the spinel-based phase during thermal treatment, although definitive determination of Fe site occupancy would require complementary advanced characterization.

3.2. Characterization of the as-prepared coatings

Cross-sectional FE-SEM observations were primarily employed to quantify coating thickness and to identify the most suitable deposition voltage within the investigated range of 30–60 V, while keeping the deposition time constant at 60 s. Cross-sections of both doped and undoped coatings subjected to different thermal treatments were analysed. A comparable microstructural arrangement was observed across all conditions, and thicknesses were systematically measured and summarised in Table 2.

The thickness data reveal a clear dependence on the applied voltage. Coatings deposited at 30 V exhibit thickness values below the 10–15 μm range selected in this work as a practical target for long-term interconnect protection. Although this

Table 2 Summary of the coating thickness values (μm) measured by cross-sectional FE-SEM for undoped (MnCu) and Fe-doped (MnCuFe) samples deposited at 30, 45, and 60 V for 60 s, after thermal treatments

Powder–voltage–time	Thickness after one step sintering [μm]	Thickness after reduction step of two steps sintering [μm]	Thickness after two steps sintering [μm]
MnCu–30 V–60 s	7.56 ± 0.4	8.07 ± 0.3	7.47 ± 0.4
MnCu–45 V–60 s	11.49 ± 0.5	13.79 ± 0.3	13.74 ± 0.3
MnCu–60 V–60 s	19.35 ± 0.8	18.84 ± 0.5	19.03 ± 0.5
MnCuFe–30 V–60 s	8.43 ± 0.3	9.59 ± 0.3	8.27 ± 0.7
MnCuFe–45 V–60 s	8.72 ± 0.4	13.04 ± 0.1	12.96 ± 0.2
MnCuFe–60 V–60 s	18.92 ± 0.5	17.1 ± 0.6	13.8 ± 0.8

range should not be regarded as a universal optimum, since the most suitable coating thickness depends on composition, processing route, microstructure, and operating conditions, similar micrometre-thick spinel coatings have been reported to be effective for protective applications on SOC interconnects.[39,56,57] Conversely, samples obtained at 60 V exceed the desired thickness window and may therefore be more prone to spallation. Since stress evolution in oxide coatings is strongly thickness-dependent, limiting excessive growth, together with controlling grain size and morphology, represents a key strategy to reduce residual stresses and improve mechanical reliability.[58,59] In contrast, coatings deposited at 45 V for 60 s consistently fall within the selected 10–15 μm target range after complete thermal treatment for both doped and undoped compositions. This condition provides the most suitable compromise between adequate barrier thickness and mechanical stability.

From a morphological standpoint, cross-sectional analysis confirms that all investigated voltages yield continuous, well-adherent coatings, with no significant differences in overall layer morphology or interface integrity.

However, the 60 V condition exhibits a less uniform microstructure, particularly in the Fe-doped samples, suggesting that higher applied fields induce rapid particle flux and non-uniform packing during deposition. Given the absence of marked qualitative differences among 30, 45, and 60 V, and considering that 45 V provides coating thickness within the selected target range, subsequent microstructural and electrochemical analyses were performed on samples deposited at 45 V for 60 s.

Fig. 3 presents representative cross-sectional micrographs of undoped, and Fe-doped coatings subjected to the different sintering treatments, clearly illustrating the microstructural evolution induced by thermal processing. After single-step oxidation (Fig. 3a and d), both MnCu_1S and MnCuFe_1S coatings exhibit good adhesion to the substrate and structural continuity across the entire thickness. Nevertheless, a relatively high residual porosity is observed compared with similar systems reported in the literature.[18,42,60,61] The addition of iron results in a finer and more homogeneous microstructure, indicating enhanced sintering kinetics and improved densification behaviour, consistent with previous studies on Fe-modified spinels.[41–43]

Following the reduction step of the two-step treatment, MnCu_Red and MnCuFe_Red samples (Fig. 3b and e) display continuous, well-defined coating layers with thicknesses of approximately 13 μm, approaching the targeted 10–15 μm range after complete thermal treatment.

The coatings remain structurally compact and adherent, with no visible evidence of elemental stratification.

Following the subsequent reoxidation step, samples MnCu_2S and MnCuFe_2S (Fig. 3c and f) show a clear increase in densification, particularly in the region adjacent to the metallic substrate. The microstructure appears more compact than that of the single-step oxidation route, indicating that the intermediate reduction promotes particle rearrangement and enhances subsequent densification during reoxidation. This behaviour can be rationalized by the phase evolution occurring during the two-step treatment: under reducing conditions, XRD analysis shows that the Mn–Cu spinel decomposes into MnO and metallic Cu, whereas subsequent reoxidation leads to reformation of the cubic spinel phase. This redox-driven transformation can enhance local cation mobility, promote particle rearrangement and neck formation, and favour the closure of residual porosity within the initially porous EPD deposit.[62,63] A thin interfacial oxide layer is visible at the coating–substrate interface, suggesting controlled oxidation of the Crofer 22 APU substrate during the thermal cycle. The 900 °C reoxidation temperature was selected based on preliminary thermal-treatment trials, which showed that lower temperatures led to coatings with higher residual porosity. Although a lower reoxidation temperature could reduce substrate oxidation and limit chromia formation, insufficient densification would compromise the barrier effectiveness of the coating against oxygen transport and chromium outward diffusion. Therefore, the selected treatment represents a compromise between coating densification and controlled interfacial oxidation.

Elemental mapping of the coatings deposited at 45 V for 60 s (Fig. 4) provides complementary compositional insight into the chemical evolution during thermal treatment.

In the MnCu_1S sample (Fig. 4a), manganese and copper are evenly distributed throughout the coating, while iron is confined to the substrate, confirming the absence of Fe diffusion during the oxidation step. In contrast, the MnCuFe_1S coating (Fig. 4b) exhibits a uniform distribution of iron within the film, demonstrating successful co-deposition and homogeneous distribution of Fe within the coating. In both cases, chromium remains confined to the steel substrate, with no

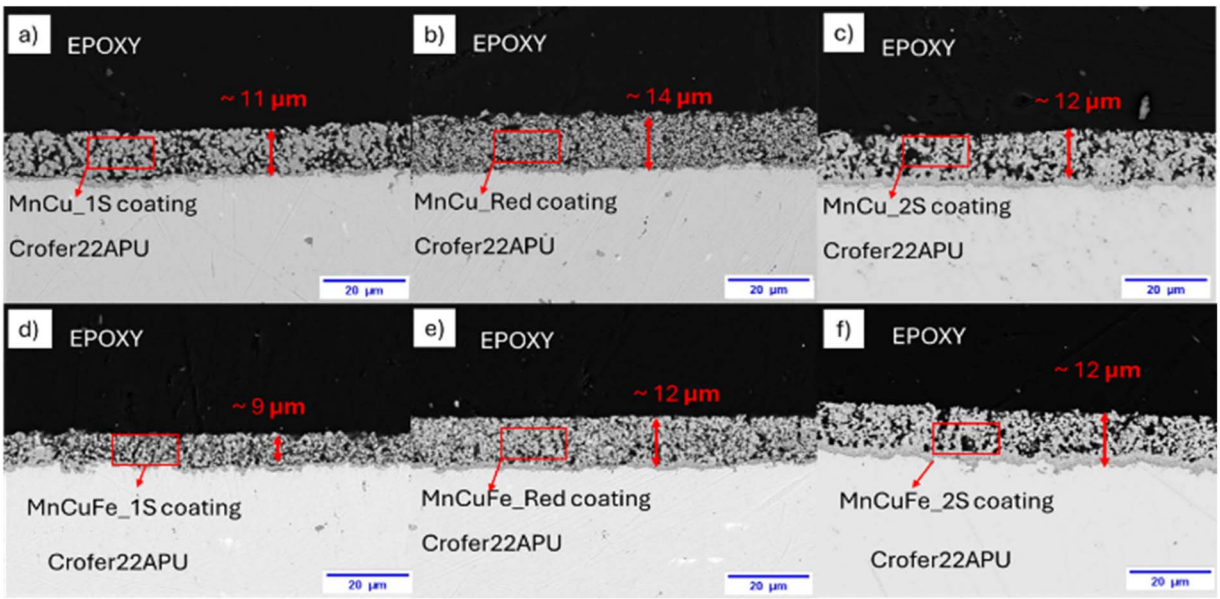

Fig. 3 FE-SEM Cross-section images (backscattered electrons) at different magnifications of coatings deposited at 45 V for 60 s after thermal treatments (a) MnCu_1S (b) MnCu_Red (c) MnCu_2S (d) MnCuFe_1S (e) MnCuFe_Red (f) MnCuFe_2S.

detectable enrichment at the interface, indicating that the single-step oxidation did not form a distinct chromia scale.

After the reduction step, the MnCu_Red coating (Fig. 4c) still indicates a continuous distribution of manganese and copper, while chromium and iron remain confined to the substrate, indicating negligible elemental interdiffusion under reducing conditions. Similarly, in the MnCuFe_Red coating (Fig. 4d), copper, manganese, and iron are evenly distributed within the film, confirming stable compositional homogeneity after reduction. Chromium remains primarily confined to the substrate, with no significant bulk diffusion into the coating, suggesting that the reducing environment effectively suppresses interfacial oxidation.

Following reoxidation, elemental maps of MnCu_2S and MnCuFe_2S (Fig. 4e and f) reveal the formation of a thin chromia layer (~1 µm) at the coating–substrate interface, characteristic of the controlled oxidation of Crofer 22 APU during high-temperature treatment.[36,43,64] No interdiffusion of the major cations (Mn, Cu, Fe) across the interface is detected, and no secondary phases are observed. Importantly, Mn–Cr spinel formation (*e.g.*, $(MnCr)_3O_4$) was not identified within the detection limit at the interface after the complete two-step sintering treatment. This differs from the behaviour reported by Ignaczak *et al.*,[43] where oxidation of ferritic stainless steel led to the formation of a dual oxide scale composed of Cr_2O_3 and an outer $(MnCr)_3O_4$ spinel layer.

Overall, the combined microstructural and compositional analyses indicate that Fe addition promotes microstructural homogenization and is consistent with incorporation into the spinel-based phase, without inducing detrimental interfacial reactions. The two-step reduction–reoxidation route enhances coating densification while maintaining controlled chromia formation at the interface, thereby benefiting long-term protective performance.

To further assess the influence of the sintering route on coating integrity and microstructural evolution, the surface morphology of both undoped and Fe-doped coatings was analysed after single-step oxidation and after the two-step reduction–reoxidation treatment.

Fig. 5 compiles representative top-view FE-SEM images for all samples, grouping undoped and Fe-doped coatings processed *via* one-step and two-step sintering, including both the reduced and reoxidized states. This arrangement allows a direct comparison between compositions and thermal schedules, highlighting the combined effect of Fe incorporation, applied voltage, and thermal treatment on surface densification and defect distribution.

All coatings are free of visible cracks, indicating that none of the applied thermal treatments compromise structural integrity. A direct comparison between MnCu_1S (Fig. 5a) and MnCuFe_1S (Fig. 5d) clearly highlights that iron addition modifies the particle morphology after sintering. In the single-step oxidation route, Fe doping results in a finer and more homogeneous surface structure, suggesting enhanced sintering kinetics and improved particle packing.

While *in situ* HSXRD provides insight into phase evolution during heating, it does not account for the effects of prolonged dwell times, redox cycling, and the specific microstructural configuration of the co-deposited coatings. In particular, HSXRD analyses were performed on powders or simple mixtures, whereas in the present work, Fe addition is achieved *via* electrophoretic co-deposition, leading to a more intimate and homogeneous distribution of the components within the coating. Therefore, *ex situ* XRD analysis is required to capture the final phase composition of the actual coating after sintering.

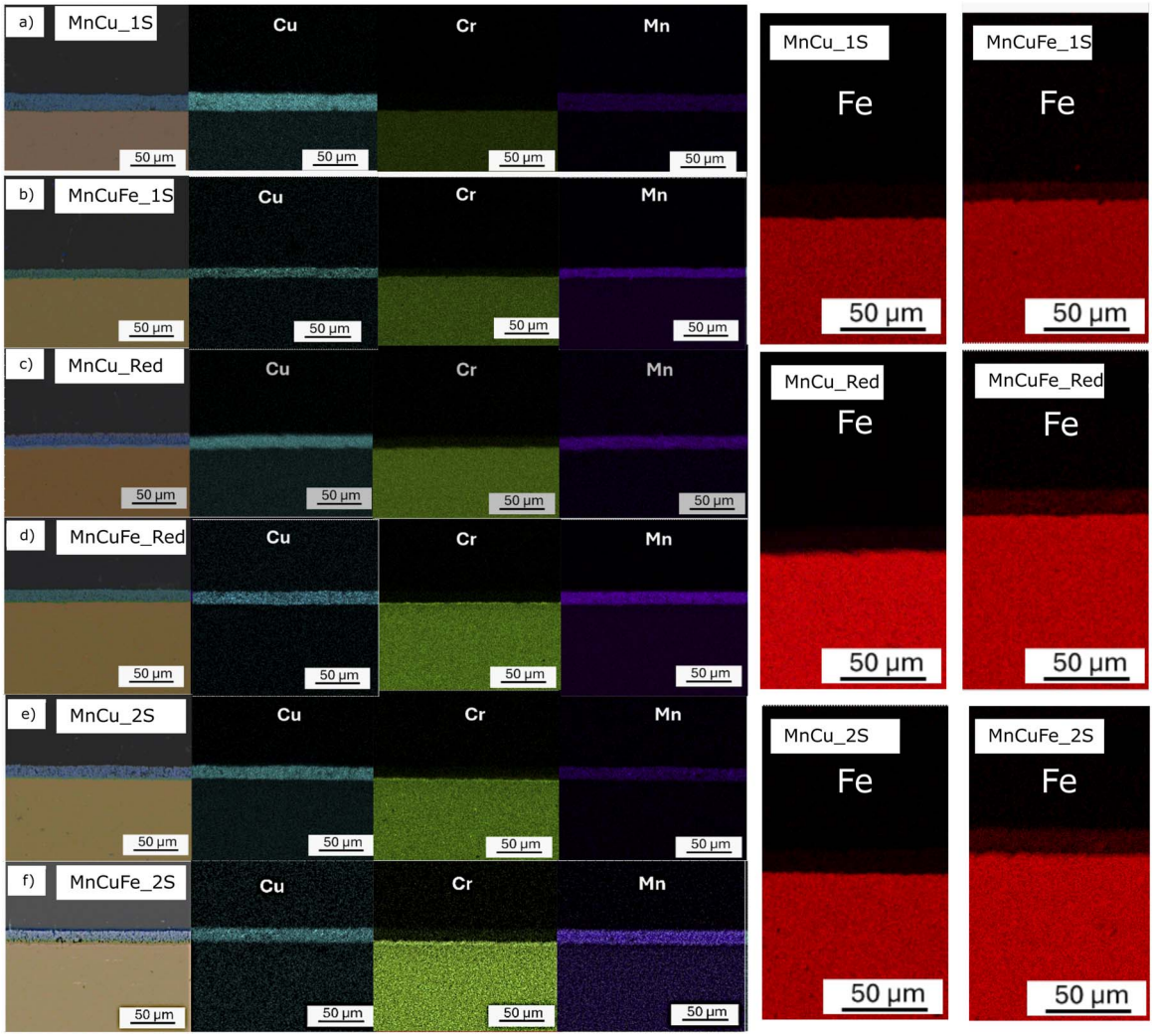

Fig. 4 EDX elemental maps of coatings deposited at 45 V for 60 s: (a) MnCu_1S (b) MnCuFe_1S (c) MnCu_Red (d) MnCuFe_Red (e) MnCu_2S (f) MnCuFe_2S. Enlarged Fe maps are included to highlight the presence of Fe in doped spinel coatings and its absence in undoped ones; the signal is dominated by the substrate due to its higher Fe content.

The XRD patterns of MnCu_1S and MnCuFe_1S coatings (Fig. 6) indicate that the single-phase cubic spinel structure is preserved in the undoped sample after thermal treatment. Minor reflections from the Fe-containing substrate are also detected, likely due to locally thinner regions of the coating. In the Fe-doped sample (MnCuFe_1S), the disappearance of Fe_2O_3 precursor peaks, together with the systematic shift of the spinel reflections, supports Fe incorporation into the Mn–Cu spinel-based phase, while a slight systematic peak shift suggests lattice parameter modification induced by Fe substitution. In the reduced state, XRD analysis (Fig. 6) confirms that the MnCu_Red coating decomposes the spinel phase into MnO and metallic Cu. A similar behaviour is observed for MnCuFe_Red, where MnO and Cu are detected, and the iron originally co-deposited as iron oxide is fully reduced to metallic Fe. This demonstrates that, under reducing conditions, the Mn–Cu spinel decomposes in both compositions, while iron is reduced without forming secondary mixed phases. The corresponding top-view images (Fig. 5b and e) show a homogeneous surface morphology in both doped and undoped coatings, with no evidence of phase segregation at the microscale.

After reoxidation (Fig. 5c and f), both MnCu_2S and MnCuFe_2S coatings exhibit well-consolidated, crack-free surfaces. Compared to the single-step oxidation process, the two-step sintering route results in enhanced surface densification, particularly in the Fe-doped configuration, without compromising coating integrity.

The reoxidized coatings display a more compact microstructure with reduced porosity, indicating that the intermediate reduction step facilitates particle rearrangement and promotes subsequent densification during reoxidation.

Finally, XRD patterns of MnCu_2S and MnCuFe_2S (Fig. 6) confirm the reformation of the cubic spinel structure in both compositions. In the Fe-doped coating, the absence of Fe_2O_3 or Fe-rich secondary phases after reoxidation supports reincorporation of iron into the spinel-based phase, consistent with the

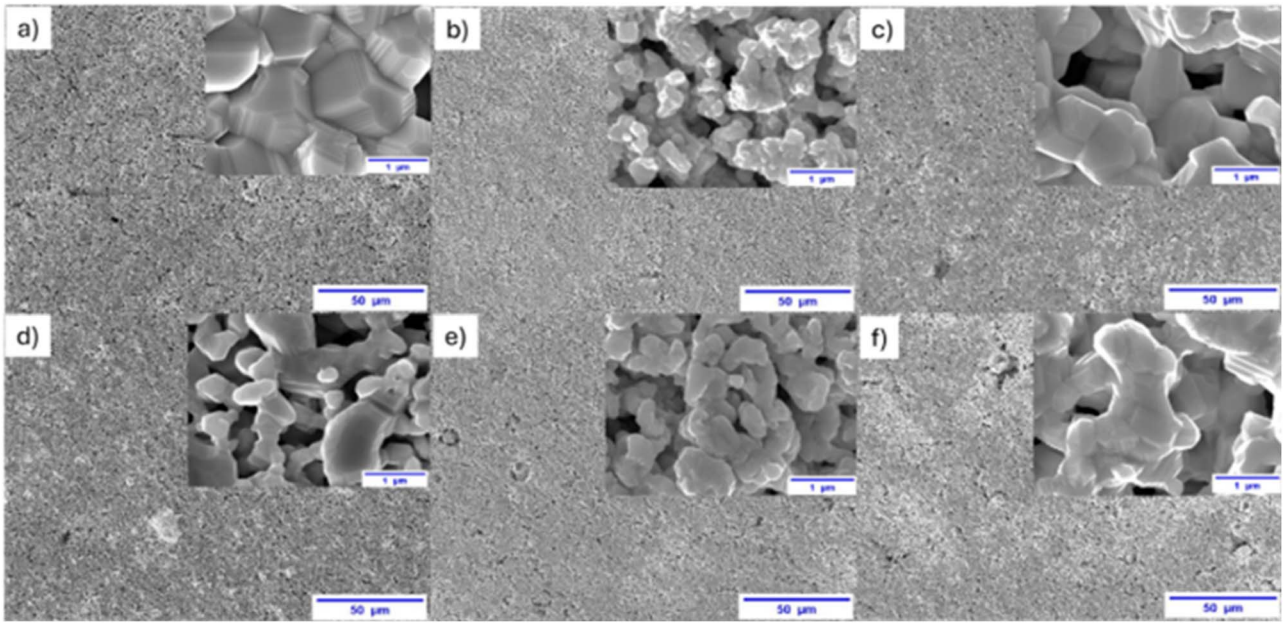

Fig. 5 FE-SEM top-view images of coatings deposited at 45 V for 60 s after thermal treatments (a) MnCu_1S (b) MnCu_Red (c) MnCu_2S (d) MnCuFe_1S (e) MnCuFe_Red (f) MnCuFe_2S.

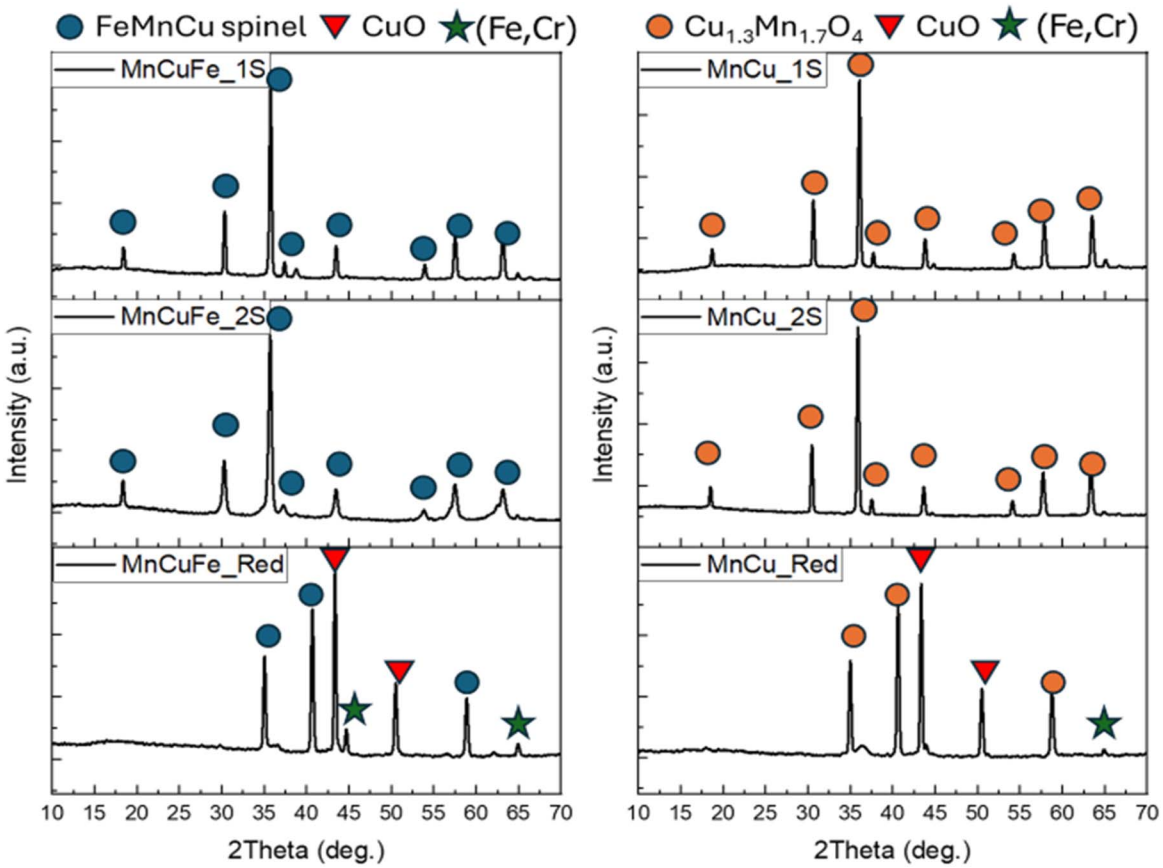

Fig. 6 XRD patterns of coatings after thermal treatments.

phase evolution observed in the single-step oxidation route. Considering the comprehensive set of microstructural, compositional, and topographic results, the MnCuFe_2S coating deposited at 45 V for 60 s emerged as the most promising candidate for further investigation. This configuration combines several advantageous characteristics: a homogeneous microstructure with reduced porosity, uniform iron distribution within the spinel matrix, a protective interfacial chromia layer, and acceptable surface roughness.

To validate the protective performance of this optimized coating under practical operating conditions, larger Crofer 22 APU sheets (5.3 cm × 5.3 cm × 0.81 mm) were coated using these selected parameters. A representative sample is shown in Fig. 7. Due to the electrical contact configuration, a partially uncoated semicircular region is visible at the top of the sample. However, electrochemical measurements were performed only on the central area, ensuring that this uncoated region did not influence the results. These samples were characterized electrochemically, as detailed in Section 3.3. Oxidation resistance tests were performed to assess the coating's effectiveness in mitigating oxide scale formation and maintaining electrical conductivity at elevated temperatures, which are critical requirements for solid oxide cell interconnects.

3.3. Electrochemical characterization

Fig. 8 shows the evolution of ASR as a function of exposure time at 850 °C under dual-atmosphere conditions (air/10% H_2 + 90% H_2O). The MnCuFe_2S-coated Crofer 22 APU interconnect exhibits initial ASR values in the 10–20 mΩ cm^2 range, followed by a moderate increase during the first few hundred hours and progressive stabilization beyond 1000 h. Overall, the measured resistance remains within the range considered acceptable for SOC interconnect operation.[19,43]

Fig. 7 Photograph of a large-area (5.3 cm × 5.3 cm) flat Crofer 22 APU interconnect coated and thermally treated.

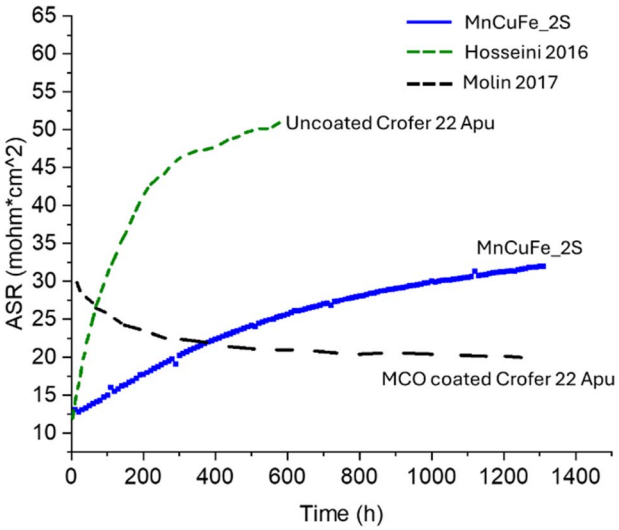

Fig. 8 Resistance of the interconnect coated with MnCuFe_2S by Polito and tested at DTU. Test condition: 850 °C, 10% H_2 + 90% H_2O supplied to the fuel electrode compartment and air supplied to the oxygen electrode compartment. The total size of the interconnector is 53 × 53 mm^2 with contact area of 40 × 40 mm^2. In the plots are reported reference values taken from the literature.[65,66]

To contextualize these results, the present dataset was benchmarked against two literature references tested in air single atmosphere at 800 °C: (i) the EPD Mn–Co spinel coating reported by Molin *et al.*,[65] and (ii) uncoated Crofer 22 APU reported by Hosseini *et al.*[66] In the study by Molin *et al.*, the EPD Mn–Co coating exhibited an initial equilibration stage over the first ∼400 h, followed by a stabilized degradation regime with a slope of approximately 1.2 mΩ cm^2/1000 h. After 5000 h, the ASR of the EPD-coated system remained around ∼22 mΩ cm^2, significantly lower than uncoated configurations.

By contrast, the uncoated Crofer 22 APU reported by Hosseini *et al.*[66] showed a continuous, pronounced increase in ASR, associated with progressive thickening of the chromia scale and the formation of poorly conductive interfacial oxides. The absence of a protective spinel layer led to substantially higher long-term resistance values than in coated systems.

Although the literature data were obtained at 800 °C, slightly lower than the 850 °C used in the present work, the comparison remains meaningful for degradation trends. Given the exponential temperature dependence of oxidation kinetics, operating at 850 °C represents a more severe condition, leading to accelerated oxide-scale growth. Achieving ASR values comparable to state-of-the-art EPD spinel coatings under these harsher conditions, therefore, highlights the effectiveness of the Fe-modified Mn–Cu coating.

A direct comparison with Mn–Co-based coated systems should nevertheless be made with caution. Mn–Cu spinels are generally reported to exhibit favourable intrinsic electrical conductivity; however, the ASR measured in an interconnect configuration is not governed solely by the intrinsic conductivity of the spinel coating. It also includes contributions from the thermally grown oxide scale, interfacial contact resistance,

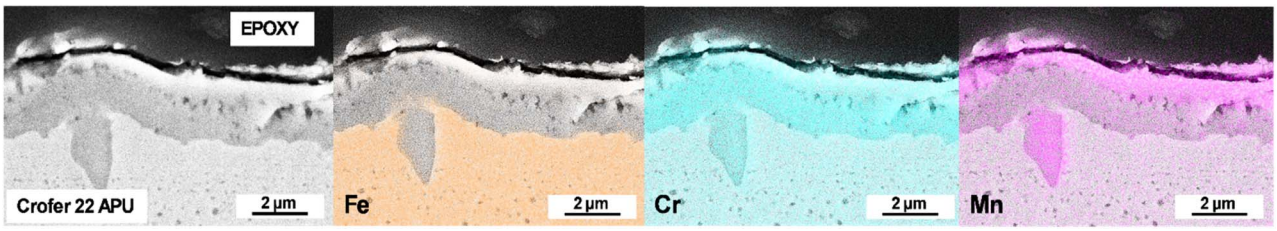

Fig. 9 SEM and EDX analysis of uncoated Crofer 22 APU facing fuel electrode compartment.

current collector/contact geometry, coating density, coating adhesion, and the specific testing atmosphere. Therefore, differences in sample geometry, coating configuration, atmosphere, temperature, and testing protocol can significantly affect the measured ASR values.

It should also be emphasized that in the present study, the MnCuFe_2S coating was applied exclusively on the air-facing side of the interconnect. The fuel-facing side, exposed to H_2 with 90% H_2O without protective coating, developed a Mn–Cr spinel layer of around 2.5 µm during long-term operation as confirmed in the EDX analysis in Section 3.4. Mixed manganese–chromium spinels exhibit significantly lower electronic conductivity compared to Mn–Co or Mn–Cu spinels and may approach the conductivity of chromia. Therefore, the measured ASR evolution cannot be attributed solely to coating degradation, but also to the contribution from the unprotected fuel side, which represents a more realistic and demanding test configuration compared to fully coated systems. The gradual ASR increase observed during long-term exposure is therefore mainly associated with the progressive evolution of oxide/reaction layers, particularly on the uncoated fuel-facing side. In addition, based on the HSXRD results, minor CuO-containing phases may form at 850 °C and could contribute to the measured resistance; however, no evidence of severe Cu-rich segregation or coating failure was observed after testing, suggesting that this is unlikely to be the dominant degradation mechanism.

Within this framework, the MnCuFe_2S system demonstrates competitive long-term performance when compared with fully coated Mn–Co systems and markedly improved behaviour relative to uncoated Crofer 22 APU.[30,67–70] The relatively limited ASR increase over more than 1300 h, despite higher temperature and single-side coating configuration, supports the reliability of Fe-modified Mn–Cu spinels as a sustainable cobalt-free alternative for SOC interconnect protection. Nevertheless, dedicated symmetrical ASR measurements, including fully coated samples tested in air and uncoated samples exposed to humidified hydrogen, will be considered in future work to decouple the individual resistance contributions of the air-facing and fuel-facing sides.

3.4. Postmortem characterization

Post-test cross-sectional SEM/EDX analyses were performed on MnCuFe_2S-coated Crofer 22 APU after long-term exposure (>1300 h) under dual-atmosphere conditions at 850 °C, to correlate microstructural evolution with the measured ASR behaviour.

3.4.1 Fuel-electrode-facing side. On the fuel-facing side, which was not protected by the MnCuFe coating and was exposed to a 10% H_2 + 90% H_2O atmosphere, oxidation of the ferritic substrate led to the formation of a multilayer oxide scale with a stratified morphology.

Cross-sectional SEM/EDX analysis (Fig. 9) reveals an inner chromium-rich layer directly above the Fe–Cr substrate, consistent with the formation of a chromia-based scale (Cr_2O_3) under high-temperature exposure. Above this layer, a manganese-enriched region is observed, indicating outward diffusion of Mn from the steel and its participation in the formation of mixed oxide phases.

Under reducing, steam-containing atmospheres, the oxygen partial pressure at the fuel side remains low of around 10^{-11} atm due to the H_2/H_2O equilibrium. These conditions are sufficient to promote selective chromium oxidation while still allowing significant cation mobility. Consequently, outward-diffusing manganese can react with chromia to form Mn–Cr spinel phases, typically identified as $(Mn,Cr)_3O_4$.[70] The formation of this mixed spinel layer is thermodynamically favoured at intermediate oxygen partial pressures and represents a common oxidation pathway for ferritic steels in SOC environments.

From an electrical standpoint, the development of a Mn–Cr spinel layer is highly relevant. While Mn–Cr spinels exhibit higher conductivity than pure chromia, their electronic conductivity remains significantly lower than that of Mn–Cu or Mn–Co spinels used as protective coatings. Consequently, the progressive thickening of this interfacial oxide structure on the uncoated fuel side increases the area-specific resistance over time.

Therefore, the ASR evolution measured during long-term testing cannot be attributed exclusively to the coated air side. A significant contribution likely arises from the gradual growth and structural evolution of the oxide scale on the unprotected fuel side, where the formation of Mn–Cr spinel and chromia layers introduces additional resistive elements into the current path. These results also indicate that coating of the fuel-side interconnect is required under high steam conditions.

3.4.2 Oxygen-electrode-facing side. On the airside, the MnCuFe_2S coating remains continuous, adherent, and free of macroscopic cracking after prolonged exposure. No evidence of delamination or through-thickness fracture is observed,

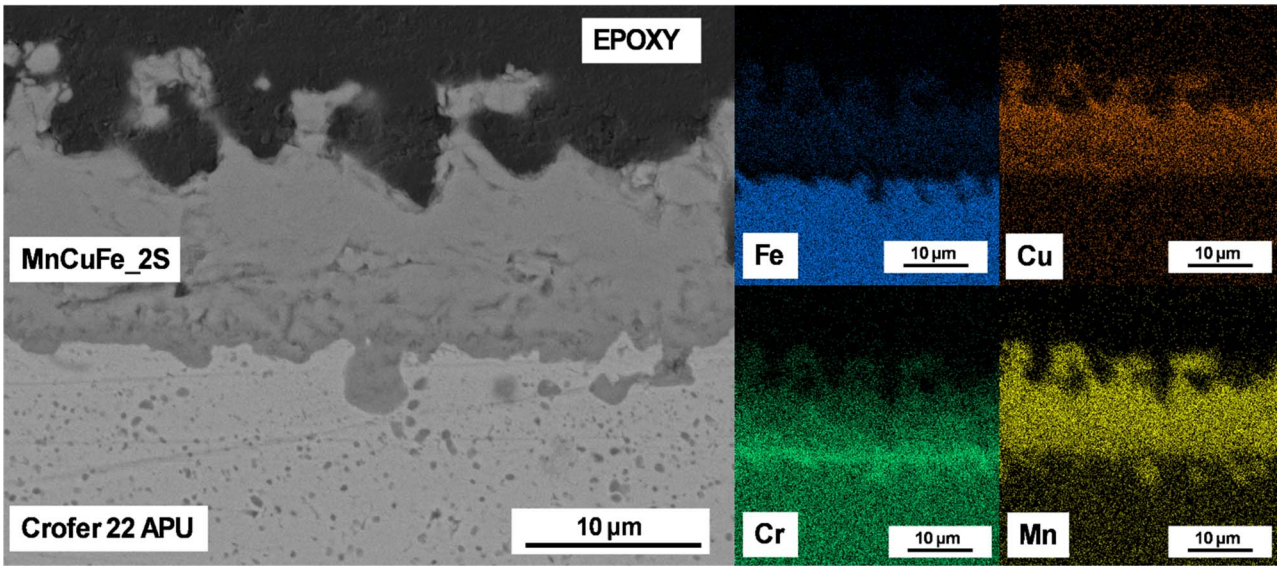

Fig. 10 SEM and EDX analysis of interconnector sample MnCuFe_2S coated facing oxygen electrode compartment.

confirming the mechanical stability of the coating produced *via* the reduction–reoxidation treatment.

Fig. 10 shows the formation of a chromium-containing reaction layer at the coating–substrate interface, along with the development of a Mn–Cr spinel phase in the interfacial region. This indicates outward diffusion of chromium from the substrate and its incorporation into the spinel structure during long-term high-temperature exposure.

The formation of Mn–Cr spinel at the air-side interface is a well-documented phenomenon in Mn-based protective coatings on ferritic steels.[71] While Mn–Cr spinels possess lower electrical conductivity than Mn–Cu or Mn–Co spinels, their presence in a thin and controlled interfacial layer can contribute to oxidation protection by acting as a diffusion barrier to further chromium transport.

Importantly, chromium incorporation is not limited to the interfacial region but extends throughout the coating thickness, indicating extensive cation redistribution during long-term exposure. At the same time, a thin chromia layer is observed at the coating–substrate interface, which is characteristic of the oxidation behaviour of ferritic stainless steels at high temperature. This combined behaviour suggests that chromium is partially accommodated within the spinel lattice while a limited amount forms a discrete chromia layer at the interface. From a functional perspective, such evolution is not necessarily detrimental. Indeed, chromium incorporated into spinel phases exhibits lower volatility compared to chromia (Cr_2O_3), thereby mitigating chromium evaporation and associated poisoning phenomena.[72] Meanwhile, a thin, controlled chromia layer can provide oxidation protection without significantly increasing overall electrical resistance. Consequently, the formation of a Cr-containing spinel across the coating, together with a limited interfacial chromia layer, can be regarded as a favorable configuration, as it stabilizes the interfacial chemistry, limits chromium volatilization, and preserves the structural integrity of the MnCuFe_2S coating.

Overall, the air-side microstructure after long-term testing reflects interfacial chemical equilibration rather than coating degradation. The moderate ASR increase observed during operation is therefore consistent with the formation of a thin Mn–Cr interfacial spinel layer and gradual scale evolution, rather than mechanical failure or catastrophic interdiffusion.

4. Conclusions

Fe-modified Mn–Cu spinel coatings were developed as cobalt-free protective layers for Crofer 22 APU solid oxide cell interconnects using a scalable electrophoretic deposition (EPD) approach.

In situ high-temperature XRD supported the thermal evolution of the Mn–Cu spinel system and indicated progressive reaction of the Fe_2O_3 precursor with the Mn–Cu spinel-based phase during thermal treatment.

Among the investigated conditions, MnCuFe_2S deposited at 45 V for 60 s provided the optimal balance between thickness (10–15 µm), compactness, and uniform cation distribution. Fe addition promoted microstructural homogenization without inducing detectable detrimental interfacial reactions.

Long-term ASR measurements performed under dual-atmosphere stack-relevant conditions at 850 °C for more than 1300 h demonstrated stable electrical performance, with ASR values remaining within the range required for SOC interconnect applications. When benchmarked against literature data for both EPD Mn–Co coatings and uncoated Crofer 22 APU tested at 800 °C, the present system exhibits competitive resistance levels despite operating at a higher temperature and tested under dual atmosphere with high steam content.

Post-mortem analyses confirmed coating integrity on the air side, controlled chromia formation at the interface, and chromium redistribution within the spinel coating without evidence of mechanical degradation. The observed increase in resistance during operation is therefore primarily attributed to oxide-scale

development on the uncoated fuel side, where Mn–Cr spinel formation increases electrical resistance.

Overall, this work demonstrates that Fe-modified Mn–Cu spinel coatings can be processed by scalable EPD and validated on large-area interconnects under realistic dual-atmosphere SOC operating conditions. The main contribution of this study therefore lies not in Fe modification alone, but in combining Fe-modified Mn–Cu chemistry with scalable coating deposition, large-area interconnect validation, long-term ASR testing, and post-mortem degradation analysis. These results extend previous material-level studies toward application-relevant interconnect testing and support Fe-modified Mn–Cu spinels as viable cobalt-free alternatives to Mn–Co protective coatings for SOC interconnects.

Author contributions

F. Gallo: conceptualization, formal analysis, methodology, investigation, visualization, writing – original draft, writing – review and editing. S. Anelli: conceptualization, supervision, writing – review and editing. F. D'Isanto: conceptualization, supervision, writing – review and editing. M. Castelli: investigation, formal analysis. X. Sun: conceptualization, supervision, writing – review and editing. A. G. Sabato: conceptualization, supervision, funding acquisition. A. Tarancón: conceptualization, supervision, funding acquisition. F. Smeacetto: conceptualization, methodology, supervision, writing – review and editing, funding acquisition.

Conflicts of interest

There are no conflicts to declare.

Data availability

All data supporting the findings of this study are included in the manuscript. Additional raw datasets are available from the corresponding authors upon reasonable request.

Acknowledgements

This work is part of the HyP3D (Hydrogen Production in Pressurized 3D-Printed Solid Oxide Electrolysis Stacks) project, funded by the European Union (Grant Agreement No. 101101274). Views and opinions expressed are however those of the author(s) only and do not necessarily reflect those of the European Union or Clean Hydrogen Joint Undertaking. Neither the European Union nor the granting authority can be held responsible for them. Dr A. G. Sabato would like to acknowledge Ramon y Cajal fellowship (RYC2021-034470-I, funded by MCIU/AEI/10.13039/501100011033 and by European Union NextGenerationEU⟫/PRTR). The authors also acknowledge support from Generalitat de Catalunya (2021-SGR-00750, NANOEN).

Notes and references

1 S. D. Tavakoli, M. G. Dozein, V. A. Lacerda, M. C. Mañe, E. Prieto-Araujo, P. Mancarella and O. Gomis-Bellmunt, *IEEE Trans. Sustainable Energy*, 2023, **14**, 2205–2219.
2 M. Khalid, *Energy Strat. Rev.*, 2024, **51**, 101299.
3 A. M. Adeyinka, O. C. Esan, A. O. Ijaola and P. K. Farayibi, *Sustainable Energy Rev.*, 2024, **11**, 26.
4 K. Hein, D. Bertin, J. Yuan, H. Zhang, V. Maquart and E. Lavillonniere, in *IECON Proceedings (Industrial Electronics Conference)*, IEEE Computer Society, 2023.
5 D. Guilbert and G. Vitale, *Clean Technol.*, 2021, **3**, 881–909.
6 A. Talukdar, A. Chakrovorty, P. Sarmah, P. Paramasivam, V. Kumar, S. K. Yadav and S. Manickkam, *Int. J. Energy Res.*, 2024, 6443247.
7 J. W. Stevenson, Z. G. Yang, G. G. Xia, Z. Nie and J. D. Templeton, *J. Power Sources*, 2013, **231**, 256–263.
8 R. Wang, Z. Sun, J.-P. Choi, S. N. Basu, J. W. Stevenson and M. C. Tucker, *Int. J. Hydrogen Energy*, 2019, **44**, 25297–25309.
9 H. S. Seo, D. W. Yun and K. Y. Kim, *Int. J. Hydrogen Energy*, 2013, **38**, 2432–2442.
10 S. P. Jiang and X. Chen, *Int. J. Hydrogen Energy*, 2014, **39**, 505–531.
11 M. Stanislowski, J. Froitzheim, L. Niewolak, W. J. Quadakkers, K. Hilpert, T. Markus and L. Singheiser, *J. Power Sources*, 2007, **164**, 578–589.
12 S. J. McPhail, S. Frangini, J. Laurencin, E. Effori, A. Abaza, A. K. Padinjarethil, A. Hagen, A. Léon, A. Brisse, D. Vladikova, B. Burdin, F. R. Bianchi, B. Bosio, P. Piccardo, R. Spotorno, H. Uchida, P. Polverino, E. A. Adinolfi, F. Postiglione, J. H. Lee, H. Moussaoui and J. Van herle, *Electrochem. Sci. Adv.*, 2022, **2**(5), e2100024.
13 Z. Zakaria, Z. Awang Mat, S. H. Abu Hassan and Y. Boon Kar, *Int. J. Energy Res.*, 2020, **44**, 594–611.
14 H. Falk-Windisch, J. E. Svensson and J. Froitzheim, *J. Power Sources*, 2015, **287**, 25–35.
15 J. C. W. Mah, A. Muchtar, M. R. Somalu and M. J. Ghazali, *Int. J. Hydrogen Energy*, 2017, **42**, 9219–9229.
16 J. Froitzheim, H. Ravash, E. Larsson, L. G. Johansson and J. E. Svensson, *J. Electrochem. Soc.*, 2010, **157**, B1295.
17 M. A. Yatoo, F. Habib, A. H. Malik, M. J. Qazi, S. Ahmad, M. A. Ganayee and Z. Ahmad, *MRS Commun.*, 2023, **13**, 378–384.
18 S. Joshi and A. Petric, *Int. J. Hydrogen Energy*, 2017, **42**, 5584–5589.
19 S. U. Oh, D. Kim, I. T. Lee, C. S. Choi, J. A. Lee, Y. W. Heo and J. H. Lee, *Int. J. Hydrogen Energy*, 2022, **47**, 33410–33419.
20 F. Smeacetto, A. De Miranda, S. Cabanas Polo, S. Molin, D. Boccaccini, M. Salvo and A. R. Boccaccini, *J. Power Sources*, 2015, **280**, 379–386.
21 E. Zanchi, J. Ignaczak, G. Cempura, S. Molin, A. R. Boccaccini and F. Smeacetto, *Mater. Lett.*, 2024, **354**, 135418.
22 W. J. Quadakkers, J. Prion-Abellan, V. Shemet and L. Singheiser, *Mater. High Temp.*, 2003, **20**, 115–127.

23 W. Z. Zhu and S. C. Deevi, *Mater. Sci. Eng. A*, 2003, **348**, 227–243.
24 C. Goebel, A. G. Fefekos, J. E. Svensson and J. Froitzheim, *J. Power Sources*, 2018, **383**, 110–114.
25 J. G. Grolig, J. Froitzheim and J. E. Svensson, *J. Power Sources*, 2015, **284**, 321–327.
26 M. Bianco, J. P. Ouweltjes and J. Van herle, *Int. J. Hydrogen Energy*, 2019, **44**, 31406–31422.
27 B. Talic, A. C. Wulff, S. Molin, K. B. Andersen, P. Zielke and H. L. Frandsen, *Surf. Coat. Technol.*, 2019, **380**, 125093.
28 B. Ferrari and R. Moreno, *J. Eur. Ceram. Soc.*, 2010, **30**, 1069–1078.
29 S. Molin, A. G. Sabato, H. Javed, G. Cempura, A. R. Boccaccini and F. Smeacetto, *Mater. Lett.*, 2018, **218**, 329–333.
30 A. G. Sabato, S. Molin, H. Javed, E. Zanchi, A. R. Boccaccini and F. Smeacetto, *Ceram. Int.*, 2019, **45**, 19148–19157.
31 B. Talic, P. V. Hendriksen, K. Wiik and H. L. Lein, *Solid State Ionics*, 2018, **326**, 90–99.
32 O. Ekhlasiosgouei, F. Smeacetto and S. Molin, *Int. J. Hydrogen Energy*, 2024, **60**, 1054–1067.
33 B. Talic, H. Falk-Windisch, V. Venkatachalam, P. V. Hendriksen, K. Wiik and H. L. Lein, *J. Power Sources*, 2017, **354**, 57–67.
34 P. Sarkar, D. De and H. Rho, *J. Mater. Sci.*, 2004, **39**, 819–823.
35 H. Sa'adati, B. Raissi, R. Riahifar and M. S. Yaghmaee, *J. Eur. Ceram. Soc.*, 2016, **36**, 299–305.
36 B. Wang, K. Li, J. Liu, T. Zhang, T. Yang and N. Zhang, *Int. J. Hydrogen Energy*, 2024, **61**, 216–225.
37 S. Molin, A. G. Sabato, H. Javed, G. Cempura, A. R. Boccaccini and F. Smeacetto, *Mater. Lett.*, 2018, **218**, 329–333.
38 E. Zanchi, B. Talic, A. G. Sabato, S. Molin, A. R. Boccaccini and F. Smeacetto, *J. Eur. Ceram. Soc.*, 2019, **39**, 3768–3777.
39 E. Zanchi, J. Ignaczak, S. Molin, G. Cempura, A. R. Boccaccini and F. Smeacetto, *J. Eur. Ceram. Soc.*, 2022, **42**, 3271–3281.
40 F. W. Schwartz, S. Lee and T. H. Darrah, *GeoHealth*, 2021, **5**, DOI: 10.1029/2020GH000325.
41 Z. Sun, S. Gopalan, U. B. Pal and S. N. Basu, *Surf. Coat. Technol.*, 2017, **323**, 49–57.
42 W. Huang, S. Gopalan, U. B. Pal and S. N. Basu, *J. Electrochem. Soc.*, 2008, **155**, B1161.
43 J. Ignaczak, L. Zeng, D. F. Sanchez, M. Makowska, K. Górnicka, K. Lankauf, J. Karczewski, P. Jasiński and S. Molin, *Int. J. Hydrogen Energy*, 2023, **48**, 36076–36093.
44 N. Hosseini, M. H. Abbasi, F. Karimzadeh and G. M. Choi, *J. Power Sources*, 2015, **273**, 1073–1083.
45 J. Ignaczak, Y. Naumovich, K. Górnicka, J. Jamroz, W. Wróbel, J. Karczewski, M. Chen, P. Jasiński and S. Molin, *J. Eur. Ceram. Soc.*, 2020, **40**, 5920–5929.
46 Ł. Mazur, K. Domaradzki, P. Winiarski, M. Bik, A. Mikuła, J. Dąbrowa, G. Cempura, A. Adamczyk, A. Kruk and T. Brylewski, *J. Mater. Chem. A*, 2025, **13**, 32741–32764.
47 VDM ® Crofer 22 APU, https://www.vdm-metals.com/fileadmin/user_upload/Downloads/Data_Sheets/Data_Sheet_VDM_Crofer_22_APU.pdf.
48 E. G. Kalinina, D. S. Rusakova and T. V. Terziyan, *Russ. J. Phys. Chem. A*, 2024, **98**, 2650–2657.
49 M. Łazor, Y. Naumovich, L. Ajdys, A. Yaremchenko, A. Żurawska and P. Wiecińska, *Int. J. Hydrogen Energy*, 2025, **120**, 613–627.
50 A. Hagen, H. Langnickel and X. Sun, *Int. J. Hydrogen Energy*, 2019, **44**, 18382–18392.
51 L. Ajdys, A. Zurawska, M. Kosiorek, Y. Naumovich, M. Zybert, P. Wiecinska and M. Chen, *Ceram. Int.*, 2023, **49**, 33818–33827.
52 E. G. Kalinina and E. Y. Pikalova, *Inorg. Mater.*, 2020, **56**, 941–948.
53 L. Besra and M. Liu, *Prog. Mater. Sci.*, 2007, **52**, 1–61.
54 A. R. Boccaccini, S. Keim, R. Ma, Y. Li and I. Zhitomirsky, *J. R. Soc. Interface*, 2010, **7**, S581–S613.
55 A. Petric and H. Ling, *J. Am. Ceram. Soc.*, 2007, **90**, 1515–1520.
56 J. Ignaczak, M. Bik, J. Jamroz, K. Górnicka, A. Drewniak, J. Karczewski, P. Jasiński and S. Molin, *J. Eur. Ceram. Soc.*, 2025, **45**, 117259.
57 M. Hilger, T. Krogsgaard, S.-M. Groß-Barsnick, D. Sebold, S. Shrikanth, J. Froitzheim, C. Lenser and N. H. Menzler, *J. Electrochem. Soc.*, 2026, **173**, 034509.
58 J. O. Carlsson and P. M. Martin, in *Handbook of Deposition Technologies for Films and Coatings: Science, Applications and Technology*, Elsevier, 2009, pp. 314–363.
59 Y. Fukada, N. Nagarajan, W. Mekky, Y. Bao, H.-S. Kim and P. S. Nicholson, *J. Mater. Sci.*, 2004, **39**, 787–801.
60 Z. Sun, R. Wang, A. Y. Nikiforov, S. Gopalan, U. B. Pal and S. N. Basu, *J. Power Sources*, 2018, **378**, 125–133.
61 R. Wang, Z. Sun, U. B. Pal, S. Gopalan and S. N. Basu, *J. Power Sources*, 2018, **376**, 100–110.
62 L. Li, X. Xin, X. Meng, T. Luo, W. Zhang, X. Ye and Z. Wen, *Int. J. Hydrogen Energy*, 2025, **124**, 386–392.
63 G. Chen, X. Xin, T. Luo, L. Liu, Y. Zhou, C. Yuan, C. Lin, Z. Zhan and S. Wang, *J. Power Sources*, 2015, **278**, 230–234.
64 Y. Liu and D. Y. Chen, *Int. J. Hydrogen Energy*, 2009, **34**, 9220–9226.
65 S. Molin, A. G. Sabato, M. Bindi, P. Leone, G. Cempura, M. Salvo, S. Cabanas Polo, A. R. Boccaccini and F. Smeacetto, *J. Eur. Ceram. Soc.*, 2017, **37**, 4781–4791.
66 S. N. Hosseini, F. Karimzadeh, M. H. Enayati and N. M. Sammes, *Solid State Ionics*, 2016, **289**, 95–105.
67 E. Zanchi, S. Molin, A. G. Sabato, B. Talic, G. Cempura, A. R. Boccaccini and F. Smeacetto, *J. Power Sources*, 2020, **455**, 227910.
68 Z. Zhu, C. Darl-Uzu, U. Pal, S. Gopalan, A. M. Hussain, N. Dale, Y. Fukuyama, Y. Miura, Y. Miyoshi and S. Basu, *Int. J. Hydrogen Energy*, 2022, **47**, 36953–36963.
69 S. N. Hosseini, F. Karimzadeh, M. H. Enayati and N. M. Sammes, *Solid State Ionics*, 2016, **289**, 95–105.
70 S. Molin, M. Chen and P. V. Hendriksen, *J. Power Sources*, 2014, **251**, 488–495.
71 K. Wang, Y. Liu and J. W. Fergus, *J. Am. Ceram. Soc.*, 2011, **94**, 4490–4495.
72 Z. Yang, G. G. Xia, X. H. Li and J. W. Stevenson, *Int. J. Hydrogen Energy*, 2007, **32**, 3648–3654.

